

Electrolyte spraying within H₂ bubbles during water electrolysis

Aleksandr Bashkatov,^{*,†,‡} Florian Bürkle,[¶] Çayan Demirkır,[‡] Wei Ding,[†] Vatsal Sanjay,[‡] Alexander Babich,[†] Xuegeng Yang,[†] Gerd Mutschke,[†] Jürgen Czarske,[¶] Detlef Lohse,^{‡,§} Dominik Krug,[‡] Lars Büttner,[¶] and Kerstin Eckert^{*,†,||}

[†]*Institute of Fluid Dynamics, Helmholtz-Zentrum Dresden-Rossendorf,
Bautzner Landstrasse 400, 01328 Dresden, Germany*

[‡]*Physics of Fluids Group, Max Planck Center for Complex Fluid Dynamics,
MESA+ Institute and J. M. Burgers Centre for Fluid Dynamics, University of Twente,
P.O. Box 217, 7500AE Enschede, Netherlands*

[¶]*Laboratory for Measurement and Sensor System Techniques,
Faculty of Electrical and Computer Engineering, Technische Universität Dresden,
Helmholtzstr. 18, 01069 Dresden, Germany*

[§]*Max Planck Institute for Dynamics and Self-Organization,
Am Fassberg 17, 37077 Göttingen, Germany*

^{||}*Institute of Process Engineering and Environmental Technology,
Technische Universität Dresden, 01062 Dresden, Germany*

E-mail: a.bashkatov@hzdr.de; k.eckert@hzdr.de

Abstract

Electrolytically generated gas bubbles can significantly hamper the overall electrolysis efficiency. Therefore it is crucial to understand their dynamics in order to optimise water electrolyzer systems. Here we demonstrate a distinct transport mechanism where coalescence with microbubbles drives electrolyte droplets, resulting from the fragmentation of the Worthington jet, into the gas phase during hydrogen evolution reaction, both in normal and microgravity environments. This indicates that the H_2 bubble is not only composed of hydrogen gas and vapor but also includes electrolyte fractions. Reminiscent of bursting bubbles on a liquid-gas interface, this behavior results in a flow inside the bubble, which is further affected by Marangoni convection at the gas-electrolyte interface, highlighting interface mobility. In the case of electrode-attached bubbles, the sprayed droplets form electrolyte puddles at the bubble-electrode contact area, affecting the dynamics near the three-phase contact line and favoring bubble detachment from the electrode. The results of this work unravel important insights into the physicochemical aspects of electrolytic gas bubbles, integral for optimizing gas-evolving electrochemical systems. Besides, our findings are essential for studying the limits of jet formation and rupture relevant to acid mist formation in electrowinning, generation of sea spray aerosols, impact of droplets on liquid surfaces, etc.

The growth of gas bubbles abounds in nature and has various engineering applications¹ and is reflected in natural phenomena. Some of them featuring rapid dynamics are sonochemistry² and sonoluminescence,³ cavitation,⁴ the evolution of CO₂ bubbles in sparkling drinks,⁵ and the bursting bubbles at the oceans surface.^{6,7} The latter contributes significantly to atmospheric aerosol generation⁸ via two different mechanisms: the disintegration of a thin liquid film between the bubble and gas interface at the onset of bursting,^{9–11} and by an inertia-driven liquid jet—referred to as Worthington jet fragmenting into multiple droplets,¹² where the mechanism is a Rayleigh–Plateau instability.¹³ Beyond aerosol generation,¹⁴ these jets are responsible for contaminant dispersion.^{15,16} Additionally, they result in surface erosion and deformation through the impact of droplets on solid¹⁷ and liquid surfaces,¹⁸ respectively.

A related problem also occurs in electrolysis, where the coalescence of hydrogen or oxygen bubbles can be approximated to bursting events at a liquid-gas interface. This is a particularly interesting problem of high practical relevance due to the prominent role of hydrogen produced via water electrolysis as an energy carrier, fuel, and feedstock for chemical and steel industries.¹⁹ Alkaline water electrolysis is still the most mature technology, albeit suffering from inadequate efficiency when operated at high current densities. A considerable part of the losses can be attributed to the formation of H₂ and O₂ bubbles, present at the electrodes and in the bulk. These bubbles mask the active area of the electrodes, reduce the number of nucleation sites, and raise ohmic cell resistance.^{20,21} Thus, enhanced removal of gas bubbles, inherently requiring a better understanding of their growth and departure, will promote continuous catalytic activity²² and benefit further optimization of the system’s energy efficiency.²³

The dynamics of electrolytic bubbles have been extensively studied in the last few decades^{20,24} to uncover the growth laws controlled by either the interfacial diffusion of dissolved hydrogen^{25,26} or direct injection of the gas at the bubble foot;²⁷ mass transfer and associated limitations;^{26,28} interactions between neighboring bubbles;^{22,29} the impact of the

electrolyte composition,³⁰ also in the presence of surfactants;³¹ the force balance governing the bubble departure^{29,32} and finally the impact of bubbles on the cell overpotentials.^{20,25} Only recently, the soluto- and thermocapillary Marangoni^{30,33–36} force and an electric^{32,37} force caused by charge adsorption, which had not been considered before, have been uncovered and quantified. Furthermore, it has been discovered that H₂ bubbles on microelectrodes do not necessarily adhere to the surface. Instead, they might reside atop a "carpet" of microbubbles and grow via intensive coalescence with this bed of tiny precursors.^{27,37} However, the full implications of such rapid coalescence events in water electrolysis remain elusive—an area ripe for further inquiry. Several lingering questions are yet to be addressed: What are the main features of the coalescence in the confined geometry, set by H₂ bubble, carpet and electrode, and how do they interact with the Marangoni flow at the bubble surface? Under what conditions does electrolytic bubble coalescence lead to droplet and spray formation? Does this affect the contact line and potentially the detachment of the electrode-attached bubble? In the present work, we address these open questions by combining experiments on the coalescence-driven dynamics of H₂ bubbles, focusing for the first time on the interior of the bubbles under both terrestrial and microgravity environments, alongside tailored direct numerical simulations.

The main phenomenon under study, spray formation *inside* a H₂ bubble during water electrolysis, is presented in Figure 1. This observation was made under microgravity conditions provided by parabolic flights of an Airbus A300.³⁸ The snapshot at $t = 0$ shown in Fig. 1a documents the time instant when the bubble sits at the electrode surface, blocking most of its active area, hindering the reaction and hydrogen production rates. Figures 1b,c respectively zoom into the bubble's central and lower segments over various time points leading up to its departure. Soon after $t = 0$, the bubble begins a lateral shift to the right driven by residual gravitational forces releasing the electrode and enabling the formation of a dense carpet of microbubbles. As a result, the primary bubble continuously coalescences with these microbubbles emerging on a time scale of $\mathcal{O}(\mu\text{s})$. The successive images

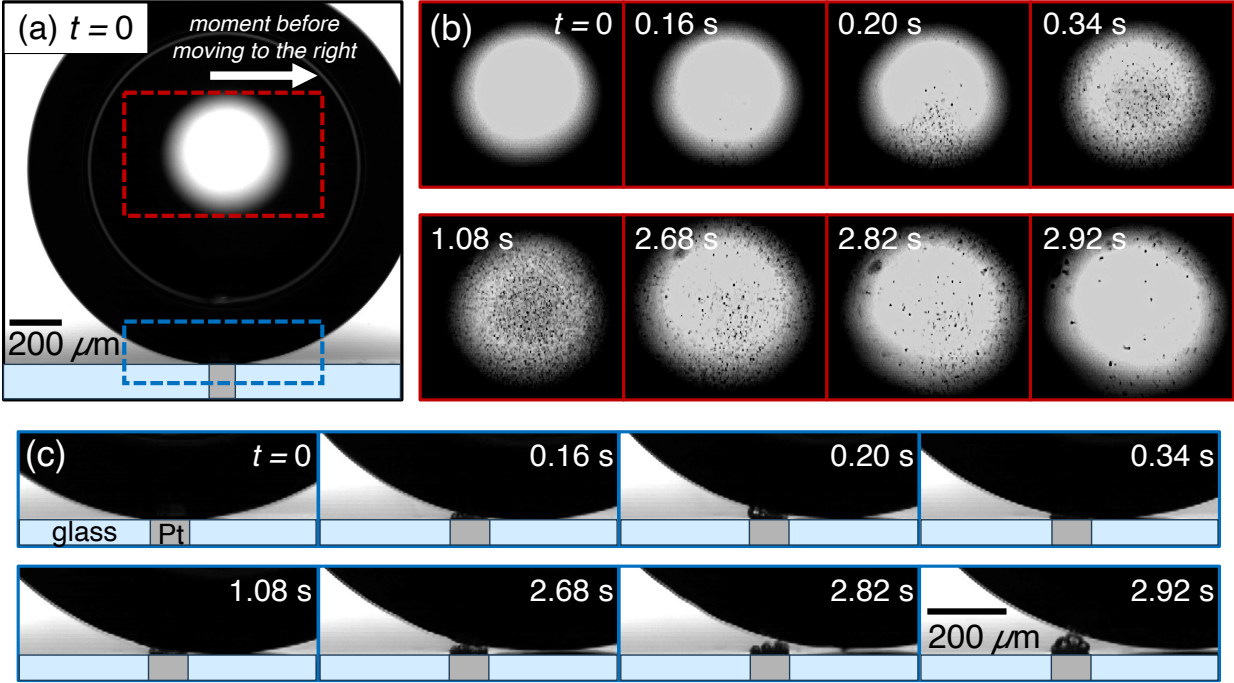


Figure 1: A series of shadowgraphs documenting the stream of electrolyte microdroplets inside a H_2 bubble ($R_b = 902 \mu\text{m}$ at the departure) during the late phase of its evolution in a micro- g environment. At $t = 0$ in (a) the bubble sits at the electrode. The successive images in (b) and (c), zooming into central and lower segments of the bubble, demonstrate the emerging flow of electrolyte microdroplets, initiated soon after the onset of lateral motion to the right followed by the intensive coalescence events. The H_2 bubble is produced during water electrolysis at $100 \mu\text{m}$ Pt micro-electrode at -4 V (vs Pt wire) in $0.5 \text{ mol/L H}_2\text{SO}_4$. The image recording was performed with a frame rate of 50 Hz .

document an emerging flow consisting of electrolyte droplets, which is initiated soon after the onset of coalescence events and ascends from the base of the bubble toward its apex. These droplets become noticeable at $t = 0.16 \text{ s}$, with their population density peaking at $t = 1.08 \text{ s}$ and declining by $t = 2.92 \text{ s}$. The gradual widening of the gap between electrode and bubble interface over time has two different effects: (i) It enhances the electrochemical reaction (by increasing the electric current, see Supplementary Section 1), thereby elevating H_2 production and bubble–carpet coalescence rates, and (ii) it leads to the generation of larger pre-coalescence bubbles, in turn decreasing the frequency of the coalescence events and, subsequently, droplet injections into the main bubble. The competition between these two effects establishes an optimal carpet thickness at which the coalescence rate has its max-

imum. Beyond this distance, the droplet population significantly reduces, as evidenced at $t = 2.92$ s. The droplet radii remain approximately constant at $1.8 \pm 0.8 \mu\text{m}$ during most of the coalescence phase, increasing to about $3.1 \pm 1.3 \mu\text{m}$ only just before bubble departure, when the gap between bubble interface and electrode is at its maximum.

In the following, we demonstrate how the phenomenon manifests itself under normal gravity conditions. Figure 2 illustrates (a) the electric current I at -3 V and -7 V, and shadowgraphs along bubble evolution at -3 V in 0.1 mol/L H_2SO_4 . In detail, a single primary bubble forms via coalescence shortly after nucleation at $t/T = 0$ from many nano- and micrometer bubbles.²⁷ It continues to grow through rapid $\mathcal{O}(\mu\text{s})$ coalescence with the carpet of microbubbles beneath. The evolution ends with the bubble departure at $t/T = 1$ when buoyancy overcomes downward forces.^{27,32} T is the bubble lifetime. $I(t)$ reflects variations in ohmic resistance due to bubble size and position relative to the electrode, peaking between the departure and nucleation of the next bubble.

In analogy to Fig. 1, numerous electrolyte droplets are injected during the coalescence events, as seen in the last image of Fig. 2a, which focuses on the central segment of the bubble at $t/T = 0.8$. The snapshots in (b,c) highlight the streaklines of the droplets over $\Delta t = 25$ ms, emerging at the bubble-carpet interface and moving towards the bubble apex with the velocities plotted in (d,e).

The flow in Fig. 2b-e develops continuously throughout the bubble evolution, along with and in response to the growing carpet thickness^{27,30} and hence elevated current, reaching velocities of up to 14 mm/s at $t/T = 1.0$. High-speed recordings at 600 kHz and 720 kHz (Supplementary Section 3) reveal that some droplets are injected at velocities up to 15.8 m/s, i.e. three orders of magnitude higher. These rare events, resulting in larger droplets, occur around the bubble's departure when the carpet thickness is at its maximum, approximately between $\delta = 16 \mu\text{m}$ and $\delta = 43 \mu\text{m}$ (see Fig. 2a), but are not observed during the earlier stages of the bubble's evolution when $\delta < 16 \mu\text{m}$.

At a substantially larger electric current (see Fig. 2a), the flow is altered by the presence

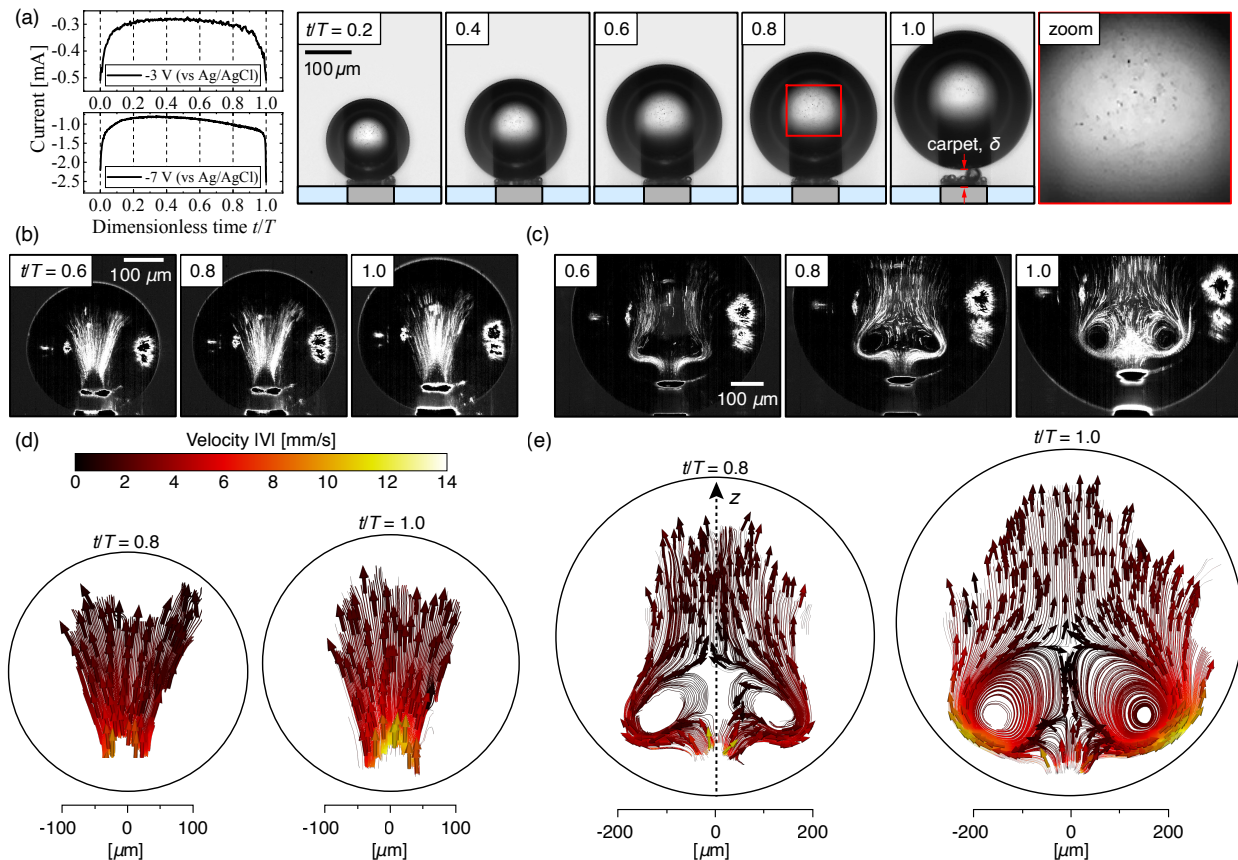


Figure 2: The dynamics of H_2 bubble presented in terms of (a) electric current at -3 V (top) and -7 V (bottom), supplemented with shadowgraphs throughout its evolution at -3 V. The most right image zooms into the middle part of the bubble at $t/T = 0.8$. (b-c) Snapshots highlighting the streaklines of the droplets over Δt . (d-e) The streamlines of the averaged drop velocity field. For the velocity calculations, the optical distortions (aberration) caused by the curvature of the bubble are corrected analytically, before the velocity calculations (Supplementary Section 2). The measurements in (b-d) and (c-e) performed in 0.1 mol/L H_2SO_4 at -3 V and -7 V vs Ag/AgCl, respectively.

of a vortical structure, see a transition from a fireworks-like shape (b,d) at -3 V to a vortex-like shape at -7 V (c,e). Meanwhile, the flow at the base of the injection remains similar. At lower potential, the flow expands away from the injection source, while at higher potential, the droplets are carried away from the injection area and ascend along the bubble-electrolyte interface. In the latter, some droplets enclosing the vortex are carried back toward the electrode. In both cases, the velocity gradually decays with distance. Indeed, the velocity of injected droplets is expected to decay exponentially over time due to viscous

drag: $V_d(t) = V_0 \cdot \exp(-t/\tau_d)$ (see Supplementary Section 4). Here, $\tau_d = \frac{m_d}{6 \cdot \pi \cdot \mu_{H_2} \cdot R_d}$ and R_d is the radius of the droplet, m_d is the mass of the droplet, V_0 is the initial velocity and μ_{H_2} is the dynamic viscosity of H_2 . For example, a droplet with $R_d = 1 \mu\text{m}$ (implies $\tau_d \approx 25 \mu\text{s}$) and initial velocity $V_0 = 5 \text{ m/s}$ slows to 10^{-2} m/s in just $160 \mu\text{s}$ by traveling $124 \mu\text{m}$. At -7 V , droplets near the z -symmetry line (see Fig. 2e) are dragged into the downward flow stream, enclosing the vortex.

The flow transition observed between -3 V and -7 V is due to Marangoni convection around an electrogenerated gas bubble existing at its outer interface. This convection originates from a gradient of surface tension caused by thermo- and/or solutocapillary effects,^{30,34,35} creating a shear stress imbalance that moves the fluid-gas interface. The resulting flow is directed alongside the electrolyte-gas interface from small to large values of surface tension, i.e., from the bottom to the top of the bubble. These effects are localized at the foot of the bubble and are consistent with the position of the vortex ring in Fig. 2e. Thermal Marangoni forces are driven by Joule heating from locally high current density (j) at the wetted part of the electrode (Fig. 5b) and scale (via Ohm's law) with j^2 , while solutal Marangoni forces arise from electrolyte depletion at the electrode and depend linearly on j . At higher potentials, as in the present study, the Marangoni convection is mainly driven by thermal effects,³⁰ with temperature rising up to 14 K .³⁵ The velocity magnitude scales with the electric current³⁴ and may reach about 10 mm/s at -2.2 mA and 47 mm/s at -4.8 mA in $0.5 \text{ mol/L H}_2\text{SO}_4$.³⁹ This concludes that the pronounced variance in flow structure between -3 V and -7 V originates from the substantial difference in electric current magnitude, and consequently, the Marangoni convection. Thus, reminiscent of evaporating droplets⁴⁰ or rising bubbles,⁴¹ Fig. 2 demonstrates for the first time that Marangoni convection at the electrolyte-gas interface drives internal flow in electrogenerated gas bubbles, directing and accelerating injected microdroplets. This also indicates that the gas-electrolyte interface is mobile, though the mechanism behind preferential ion adsorption and its effects remain unclear.

Another intriguing outcome of the spraying, shown in Figure 3, is the formation of electrolyte fractions within an electrode-attached and growing H_2 bubble, specifically at the contact area with the electrode surface.^{29,31} Figure 3a,b,d documents the views from below a transparent planar electrode (20 nm of Pt). The snapshots in Fig. 3b zoom in on the contact patch (area marked by the red rectangular in Fig. 3a), which is seen to feature sessile electrolyte droplets inside the gas phase, that expands throughout the bubble evolution.²⁹ The bubble grows mainly due to diffusion of the dissolved gas but also via coalescence with the neighboring bubbles. Here, the smaller bubbles nucleate below the equator of the primary bubble and quickly detach, see a plume of out-of-focus small bubbles in Fig. 3a, likely due to the altered morphology/wettability of a tiny cavity they nucleated at. Consequently, upon reaching the gas-liquid interface of the larger bubble, coalescence occurs between the two, see schematic in Fig. 3c.

Figure 3d details the injection of at least two microdroplets, marked by red and green arrows, following the coalescence event between the primary and smaller bubble (black arrow at $t = 0$). The first droplet (red arrow) moves with a much faster velocity, likely shooting through the gas-electrolyte interface on the opposite side. In contrast, the second droplet, about $r = 4 \mu\text{m}$ (green arrow), slows down quickly due to Stokes’s drag (Supplementary Section 4) and falls, presumably at terminal velocity, to the contact patch at $t = 86.67 \text{ ms}$, merging with another droplet. – In detail, it moves with an average velocity of about $\bar{V}_d = 0.26 \text{ m/s}$ within the first 1.33 ms and about $\bar{V}_d = 6 \text{ mm/s}$ between 1.33 ms and 86.67 ms, assuming the traveled distance S_d equals the bubble radius $R_b = 509 \mu\text{m}$. The latter correlates well with the terminal velocity of the droplet $V_t = 4.1 \text{ mm/s}$ in the Stokes regime (Supplementary Section 4). The process repeats during numerous coalescence events, resulting in the gradual formation of electrolyte puddles as shown in Fig. 3b. These puddles grow in size throughout the bubble evolution, as more electrolyte droplets are injected, wetting larger areas of the electrode. Once any of the puddles reaches the gas-electrolyte interface, it rapidly merges with the electrolyte bulk, thereby moving the contact line and

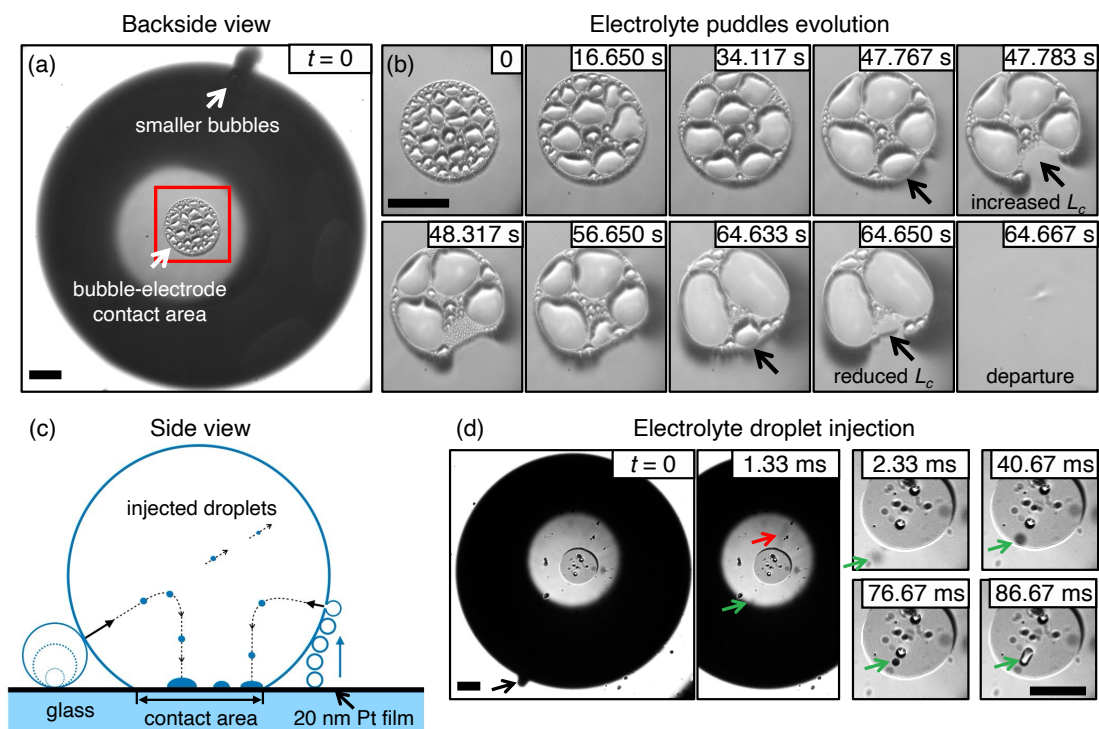


Figure 3: (a,b,d) Backside views from underneath the electrode of the growing H_2 bubble attached to the transparent planar Pt electrode. (b) Zooms into the bubble-electrode contact area shown by the red rectangular in (a), demonstrating the development of electrolyte puddles throughout the bubble evolution. (c,d) Schematic and shadowgraphs illustrating the injection of microdroplets upon coalescence events followed by their sedimentation at the contact area. Scale bars are $100 \mu\text{m}$. The measurements were carried out at a current density of 50 A/m^2 in 0.1 mol/L HClO_4 . The image recording in (a,b) and (d) was performed at frame rates of 60 Hz and 3000 Hz , respectively.

effectively reducing the bubble-electrode contact area (see frames at 47.783 s and 64.650 s).

This process thus plays a key role for the bubble detachment. The detachment size of an electrode-attached bubble is primarily governed by the surface tension force F_s , which depends on the length of the contact line (L_c). Comparing the snapshots at 47.783 s and 64.650 s , the length of the contact line can either increase or decrease after the puddle merges into the electrolyte bulk. A sudden reduction in L_c , provided there is sufficient buoyancy, causes an earlier detachment from the electrode surface, as illustrated in the snapshot at 64.667 s . The scarcity of electrolyte puddles in (d) is attributed to the reduced number of nucleation sites and their lower activity near the primary bubble, resulting in a lower

frequency of coalescence events and fewer injected droplets.

Figure 4a shows a sequence of shadowgraphs detailing the mechanism of droplet injection characterized by the formation of an internal jet that entrains a volume of electrolyte, known in the fluid mechanics and physical oceanography communities as the Worthington jet.⁴² The process is demonstrated by two coalescing H₂ bubbles with sizes $R_b = 400 \mu\text{m}$ and $R_s = 205 \mu\text{m}$, respectively. The results are corroborated by direct numerical simulations (DNS) shown in Fig. 4b. In detail, when a smaller bubble touches a larger one, the liquid film that separates the bubbles gradually drains, forming a neck connecting the two ($t = 33.3 \mu\text{s}$).⁴³ Growth of this neck follows a Taylor–Culick-type mechanism^{44–46} exciting capillary waves that propagate along the bubble interface,^{47,48} see $t = 66.7 \mu\text{s}$ to $183.3 \mu\text{s}$. The viscous forces dictate the motion of these capillary waves enervating all but the strongest (with highest curvature) waves that ultimately focus at the bottom and induce a region of high curvature,^{49–51} see $t = 191.7 \mu\text{s}$ to $208.3 \mu\text{s}$. This inertial flow focusing creates an upward jet ($t = 216.7 \mu\text{s}$ to $241.7 \mu\text{s}$)^{48,51,52} propagating inside of the merging H₂ bubbles. Consequently, this process is controlled by the dimensionless viscosity of the electrolyte given by the Ohnesorge number Oh

$$Oh = \frac{\mu_{el}}{\sqrt{\rho_{el}\gamma R_s}}, \quad (1)$$

where μ_{el} represents the dynamic viscosity, ρ_{el} the density of the electrolyte, γ the surface tension, and R_s the initial radius of the smaller bubble. Eventually, the jet breaks into two droplets due to the Rayleigh–Plateau instability,^{50,51} for $Oh < Oh^*$ where $Oh^* \approx 0.035$ is the critical Ohnesorge number for drops–no-drops transition^{50,51} for bursting at the liquid–gas free interface. Beyond the critical Ohnesorge number, viscous dissipation dominates, ceasing the ejection of drops. On further increasing the Ohnesorge number ($Oh > 0.1$), the Worthington jet does not form.^{50,51}

The DNS results in Fig. 4b accurately reproduce key features and timescales of the phenomenon such as neck formation, capillary wave propagation, formation, and breakup of

the jet. In the experiments, the first droplet with a radius of $r_d = 13 \mu\text{m}$ is observed at $t = 250.0 \mu\text{s}$ and ejects with a velocity of approximately $\bar{V}_d = 7.2 \text{ m/s}$. In close qualitative and quantitative agreement, the simulation demonstrates the first droplet (radius $r_d = 15 \mu\text{m}$) pinching off at $t = 260 \mu\text{s}$ with $\bar{V}_d = 4.3 \text{ m/s}$. Further details and discussion on the origins of minor quantitative discrepancies are elaborated in Supplementary Section 5.

It is important to note that the injection demonstrated at $Oh = 0.008$ in Fig. 4 represents a relatively isolated but conventional case,^{50,51} with the smaller bubble being located far from the electrode. In contrast, the bursting events in Figs. 1 and 2 taking place in a highly confined configuration near the Pt electrode feature high coalescence rates and involve smaller bubbles (up to about $R_s = \delta/2 = 8 \mu\text{m}$). Despite the higher Ohnesorge number ($Oh = 0.042$), injections still occur, exceeding the critical Oh^* found for an unconfined isolated bubble. This observation suggests that a nearby wall and high coalescence rates can significantly influence the injection mechanism. In agreement with this, Lee et al. (2011)⁵³ identified a higher critical value $Oh^* = 0.052$, specifically for smaller bubbles ($Bo < 10^{-3}$) bursting near a solid boundary. We refer the readers to Sanjay et al. (2024)⁵⁴ for further details.

Lee et al. (2011)⁵³ also studied a bubble with a relatively small $R_s = 26.5 \mu\text{m}$ adjacent to a Pt substrate using ultrafast X-ray imaging, finding daughter aerosol droplets ($2 \mu\text{m}$ to $4 \mu\text{m}$ radii) with velocities around 0.3 m/s (Supplementary Movie 5 in Lee et al.⁵³). Consequently, we can classify the bursting events in order of increasing droplet speed: (i) carpet bubbles ($R_s = 8 \mu\text{m}$) bursting near a solid wall with a velocity of $V_d \sim 10^{-2} \text{ m/s}$, (ii) a bubble with $R_s = 26.5 \mu\text{m}$ bursting near the solid wall, resulting in a droplet speed of $V_d \sim 10^{-1} \text{ m/s}$, and (iii) the bubble with $R_s = 205 \mu\text{m}$ bursting away from the wall (as detailed in Fig. 4), which results in a droplet speed in the range of $V_d \sim 10^0 \text{ m/s}$ to 10^1 m/s . Further deceleration likely comes from viscous drag within the surrounding H_2 gas, as described by the Oseen approximation to the Stokes flow.⁵⁵ Finally, a high coalescence rate, as seen in Figs. 1 and 2, could disrupt the symmetry of coalescence, affecting the propagation of capillary waves in each event and potentially significantly reducing the velocity of the ejected droplets to

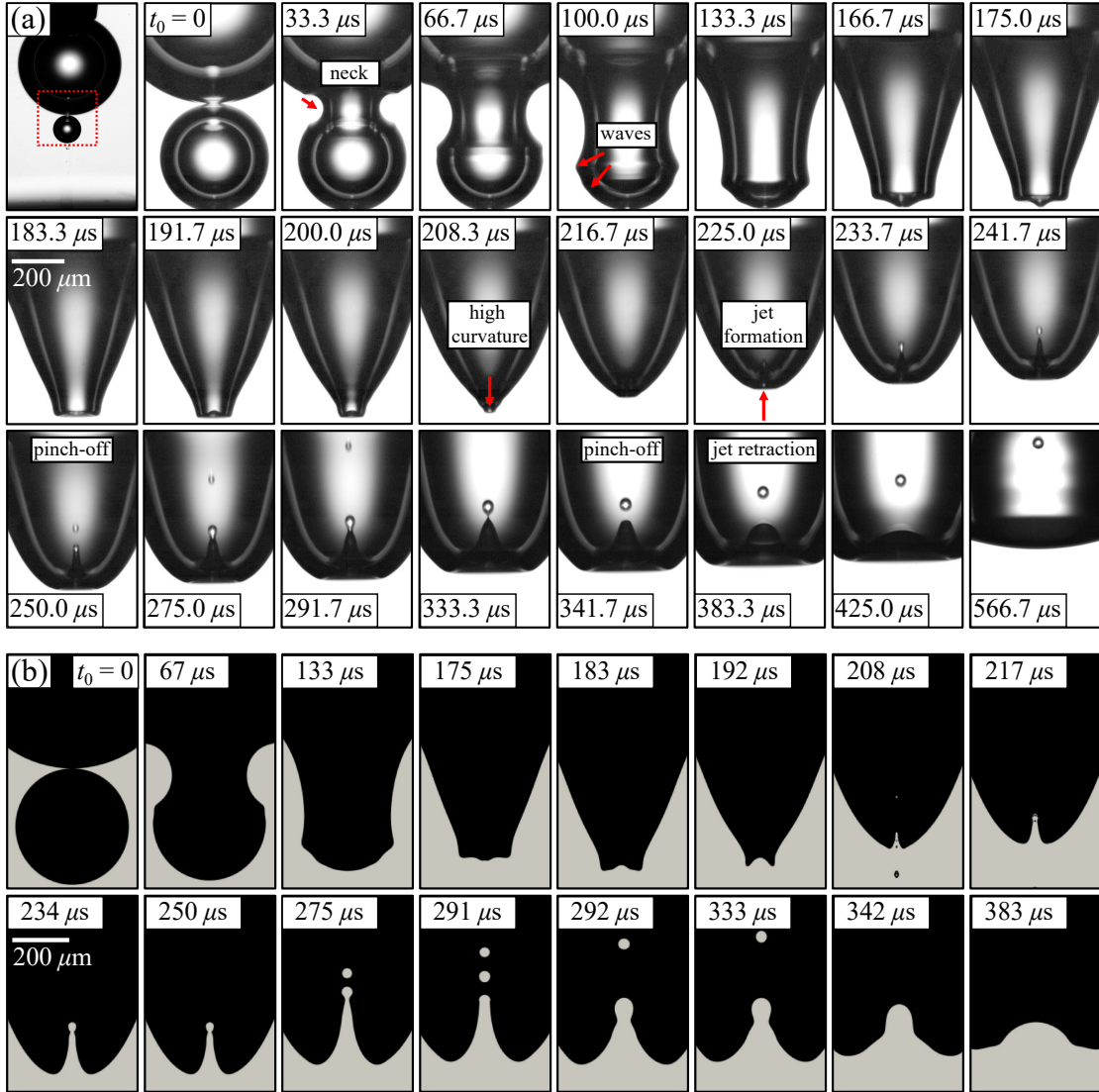


Figure 4: Droplet ejection mechanism upon coalescence of two unequal size H_2 bubbles shown by snapshots from (a) experiment and (b) numerical simulation. In the experiment, both bubbles were produced during electrolysis in $0.5 \text{ mol/L H}_2\text{SO}_4$. While the bigger bubble is pinned to a blunt needle, the smaller bubble rises from the electrode until the coalescence begins at $t_0 = 0$. The coalescence process is accompanied by the injection of two droplets after their consecutive separation from the jet. The first snapshot in (a) demonstrates the configuration marking the region of interest by the red square. The image recording was performed at 120 kHz .

$V_d \sim 10^{-2} \text{ m/s}$. Therefore, the small initial size of the bursting bubble (i.e., large Oh), proximity to a wall, higher viscosity of the gas bubbles, and potentially high coalescence rates can substantially reduce the injection velocity.

Our findings demonstrate a distinct transport mechanism of electrolyte droplets inside the gas phase during water electrolysis. As discussed above, the coalescence of a primary bubble with the bubbles-satellites causes the electrolyte spraying via the fragmentation of the Worthington jet. This indicates that the H₂ bubble is not only composed of hydrogen gas and vapor but includes electrolyte fractions given the coalescence with nearby bubbles. We emphasize again that the microdroplets formed in the bubble through this process play an important role for the bubble detachment, once they merge with the surrounding electrolyte at the contact line. The results we report will be integral for further studying the limits of jet formation and rupture associated with Oh^* in confined geometries near a solid boundary. Additionally, our findings will be valuable for validating and tailoring numerical and theoretical models. We highlight that the injected droplets serve as a non-invasive tool, making the internal flows associated with Marangoni convection at the electrolyte-gas interface visible and quantifiable for the first time. This gives access to the important surface mobility of electrogenerated bubbles, which is determined by preferential ion adsorption — a phenomenon that remains poorly understood. This will allow to access the role of physicochemistry in the hydrodynamic phenomena related to bubbles. The knowledge could further be transferred to the other side of the electrochemical reaction — the formation of O₂ bubbles. The results of this work unravel important insights into the physicochemical aspects of electrochemically generated H₂ gas bubbles and have broad relevance, e.g. to acid mist formation in electrowinning processes;⁵⁶ the generation of sea spray aerosols,⁶ which play a role in airborne disease and pollutant transmission;¹⁶ bursting CO₂ bubbles in sparkling drinks;⁵ and to the impact of droplets on liquid¹⁸ surfaces. In particular, the findings are essential for the water electrolysis field, where a deeper understanding of bubble evolution mechanisms is essential for optimizing gas-evolving electrochemical systems.

Methods

The hydrogen gas bubbles were produced using both micro- and planar electrodes during water electrolysis. Part of the results (see Fig. 1) were obtained in a microgravity environment achieved during the 34th DLR Parabolic Flight Campaign in September 2019 (see Bashkatov et al.³⁸).

Microelectrode system

Single hydrogen gas bubbles growing on the carpet of microbubbles were produced using a three-electrode electrochemical cell filled with sulfuric acid of either 0.1 mol/L or 0.5 mol/L concentration, see Fig. 5a. It comprises a cathode (Pt microelectrode, $\varnothing 100 \mu\text{m}$, ALS Co., Ltd) inserted horizontally facing upward in the base of a transparent cuboid glass cuvette (Hellma) with dimensions of $10 \times 10 \times 40 \text{ mm}^3$, anode (Pt wire, $\varnothing 0.5 \text{ mm}$) and a reference electrode (Ag/AgCl) both inserted from the top. The experiments in a microgravity environment were done using a pseudo-reference electrode (identical to the anode).³⁸ The electrochemical cell was fixed inside an outer housing featuring two optically accessible observation windows. Before the measurements, the microelectrode surface underwent mechanical polishing with sandpaper (2000 grit), sonication, and rinsing with ultrapure water. For microgravity experiments, it was polished by diamond ($1 \mu\text{m}$) and alumina ($0.05 \mu\text{m}$) suspensions (ALS Co., Ltd) instead. The cell was connected to an electrochemical workstation (CHI 660E) and operated at a constant potential of either -3 V , -4 V or -7 V .

The experiments using a blunt needle in Figure 4 were performed as follows. First, a larger H_2 bubble with a radius of approximately $400 \mu\text{m}$ was generated at the microelectrode and then detached following a potential interruption. As it rose, it adhered to a blunt needle positioned above the microelectrode, with surface tension keeping the bubble attached. A second, smaller bubble with a radius of approximately $205 \mu\text{m}$ was created in the same manner, with the smaller size achieved by applying a shorter pulse of potential. As this

smaller bubble rose, it contacted the larger bubble, initiating the coalescence process. The time t_0 marks the moment just before coalescence begins.

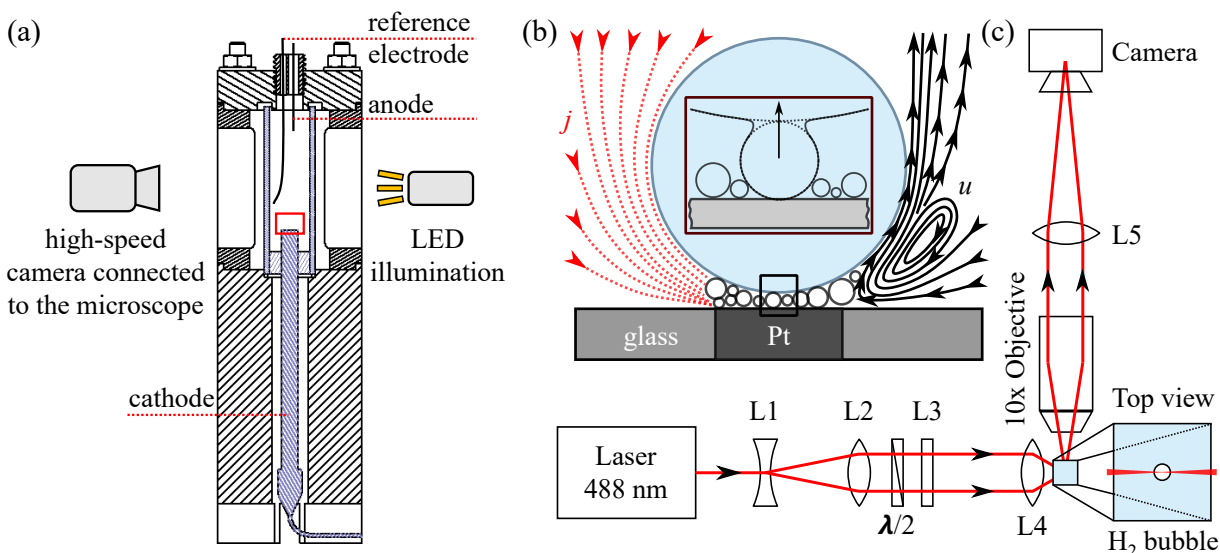


Figure 5: Schematics (not to scale) of (a) an electrochemical cell and a shadowgraphy system; (b) H₂ bubble sitting on the carpet of microbubbles generating between its bottom and electrode surface. Inset zooms into the bottom of the bubble where an intensive bubble-carpet coalescence takes place; (c) PTV optics used to measure the velocity of the injected droplets inside the H₂ bubble. For details see text.

Planar electrode system

The electrode-attached hydrogen gas bubbles were produced at the surface of a $\varnothing 50$ mm disc-like planar electrode (cathode) inserted horizontally facing upward in the base of the cylindrical PTFE compartment with an inner diameter of 40 mm and a height of 50 mm filled with 0.1 mol/L HClO₄. The cathode was fabricated by sputtering a 20 nm thin film of platinum onto a glass slide, with a 3 nm tantalum layer applied for improved adhesion. The thin layer of platinum ensured the transparency of the cathode and allowed the visualization from the bottom of the cell. The cell was completed by a platinized titanium mesh (anode) and the Ag/AgCl reference electrode both inserted from the top. The system was controlled by the electrochemical workstation (Biologic VSP-300) maintaining a constant current density of 50 A/m². The relatively low current density and smooth surface of the cathode allowed

only a limited number of active nucleation sites, making the study of the contact line and electrolyte puddles dynamics possible. For details, we refer to Çayan Demirkır et al.²⁹.

Shadowgraphy system

The visualization of the bubble dynamics is performed using a conventional shadowgraphy system, shown schematically for a microelectrode system in Figure 5a. It consists of a high-speed camera connected to the microscope and LED illumination. The shadowgraphs in Figs. 1 and 2a were recorded using an IDT camera (NX4-S1 and Os7-S3) with spatial resolutions of 678 pixels/mm and 1000 pixels/mm, respectively. In Figs. 3 and 4a, a Photron camera (FASTCAM NOVA S16) was used, with spatial resolutions of 530 pixels/mm and 496 pixels/mm, respectively. To achieve the bottom view (planar electrode system), the optical path of a horizontally installed camera is redirected vertically through the transparent cathode using a 45° mirror mounted below the electrode.²⁹ The LED light illuminates perpendicularly to the electrode from the top of the cell. The vertical adjustments of the focal plane are achieved using a high-precision motorized stage.

Particle Tracking Velocimetry (PTV)

The evolution of H₂ bubbles at microelectrodes is featured by the intensive coalescence with the carpet of microbubbles sandwiched between the bubble bottom and electrode (Fig. 5b) on a time scale of μ s. Owing to these coalescence events, multiple electrolyte droplets are injected into the bubble. The velocity measurement of these electrolyte droplets is performed using a Particle Tracking Velocimetry (PTV) system, schematically shown in Figure 5c.

The setup employs a light sheet optical configuration comprising a laser (OBIS 488LX, 150 mW, Coherent Inc.) that was spatially enlarged using a telescope (L1 & L2). To minimize reflection at the bubble surface, a $\lambda/2$ -waveplate is employed to rotate the polarization. Subsequently, the beam is vertically expanded using a cylindrical lens (L3) before being focused inside the bubble by another lens (L4) with a focal length $f = 19$ mm. For imaging

purposes, a microscope objective (PLN 10X, Olympus) is positioned such that the bubble resides within the working distance. Finally, the bubble is imaged onto the camera (EoSens 3CXP, Mikrotron) using a lens (L5) with a focal length $f = 160$ mm. To resolve the contours of the bubble, the system additionally possesses a background LED illumination. A series of images from Fig. 2b-c is collected at 1 kHz having a spatial resolution of 1140 pix/mm. The resulting series of images were processed by the software DaViS 10, which employs a Particle Tracking Velocimetry (PTV) algorithm to track each particle (droplet) over 25 ms at $t/T = 0.6, 0.8$ and 1.0 . Due to the limited number of droplets, the resulting tracks were collected over several bubbles. Subsequently, the tracks were converted into a vector field using a binning function that interpolates local tracks on a specified fine grid. Finally, the vector fields are used to plot the streamlines of the averaged drop velocity field shown in Fig. 2.

Numerical method

In this work, the direct numerical simulation code, Basilisk, is employed to simulate the coalescence of two bubbles. A two-fluid model, combined with a Navier Stokes solver, is employed. The interface of the liquid and gas is tracked with the Volume of Fluid (VOF) method. The liquid phase is water with a density and dynamic viscosity of 1000 kg/m^3 and $0.00105 \text{ Pa}\cdot\text{s}$, respectively. The gas phase is air, with a density and dynamic viscosity of $1.41 \text{ kg}\cdot\text{m}^3$ and $1.46 \cdot 10^{-5} \text{ Pa}\cdot\text{s}$. The surface tension on the interface of liquid and gas is 0.072 N/m . The initial radius of bubble 1 is $R_b = 400 \mu\text{m}$ and bubble 2 is $R_s = 200 \mu\text{m}$. Figure 6 demonstrates a sketch of the simulation model.

Spatial discretization is performed using a quad-tree method in a 2D axisymmetric calculation domain of $1.5 \cdot 10^{-3} \text{ m} \times 1.5 \cdot 10^{-3} \text{ m}$. The adaptative Mesh Refinement algorithm was used to increase the calculation accuracy and reduce the hardware requirement. The maximum refinement level and the minimum level are 9 and 5, respectively. The calculation time step size is set to $1 \cdot 10^{-8} \text{ s}$.

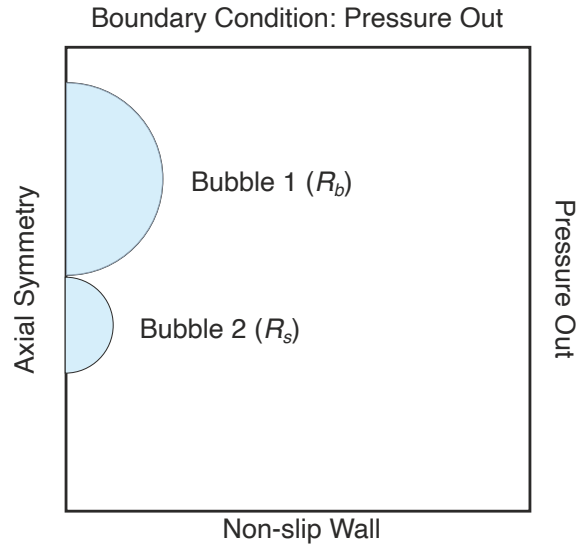


Figure 6: Sketch of the simulation model.

Acknowledgements

This research received funding from the German Space Agency (DLR), with funds provided by the Federal Ministry of Economics and Technology (BMWi) due to an enactment of the German Bundestag under Grant No. DLR 50WM2352 (project MADAGAS III), H2Giga (BMBF, 03HY123E), from the Hydrogen Lab of the School of Engineering of TU Dresden, from the Advanced Research Center Chemical Building Blocks Consortium (ARC CBBC), under the project of New Chemistry for a Sustainable Future (project number 2021.038.C.UT.14) and partially from the German Research Foundation (DFG, project number 459505672).

Author contributions

A.B. and K.E. conceived the project. A.B., F.B., Ç.D., A.B., X.Y., D.L., D.K., L.B. and K.E. designed the experiments. A.B., F.B., Ç.D. and X.Y. carried out the experiments. W.D. and V.S. carried out numerical simulations. A.B., Ç.D., W.D., V.S., A.B., G.M., J.C, D.L., D.K. and K.E. carried out bubble dynamics analysis. All authors read and commented

on the manuscript. All authors approved the final version of the manuscript.

Competing interests

The authors declare no competing interests.

References

- (1) Lohse, D. Bubble puzzles: from fundamentals to applications. *Physical Review Fluids* **2018**, *3*, 110504.
- (2) Suslick, K. S. Sonochemistry. *Science* **1990**, *247*, 1439–1445.
- (3) Brenner, M. P.; Hilgenfeldt, S.; Lohse, D. Single-bubble sonoluminescence. *Reviews of Modern Physics* **2002**, *74*, 425.
- (4) Obreschkow, D.; Kobel, P.; Dorsaz, N.; De Bosset, A.; Nicollier, C.; Farhat, M. Cavitation bubble dynamics inside liquid drops in microgravity. *Physical Review Letters* **2006**, *97*, 094502.
- (5) Liger-Belair, G.; Polidori, G.; Jeandet, P. Recent advances in the science of champagne bubbles. *Chemical Society Reviews* **2008**, *37*, 2490–2511.
- (6) Villermaux, E.; Wang, X.; Deike, L. Bubbles spray aerosols: Certitudes and mysteries. *PNAS Nexus* **2022**, *1*, pgac261.
- (7) Deike, L. Mass transfer at the ocean–atmosphere interface: the role of wave breaking, droplets, and bubbles. *Annual Review of Fluid Mechanics* **2022**, *54*, 191–224.
- (8) Blanco-Rodríguez, F. J.; Gordillo, J. On the sea spray aerosol originated from bubble bursting jets. *Journal of Fluid Mechanics* **2020**, *886*, R2.

- (9) Lhuissier, H.; Villermaux, E. Bursting bubble aerosols. *Journal of Fluid Mechanics* **2012**, *696*, 5–44.
- (10) Rage, G.; Atasi, O.; Wilhelmus, M.; Hernández-Sánchez, J. F.; Haut, B.; Scheid, B.; Legendre, D.; Zenit, R. Bubbles determine the amount of alcohol in Mezcal. *Scientific Reports* **2020**, *10*, 11014.
- (11) Jiang, X.; Rotily, L.; Villermaux, E.; Wang, X. Abyss Aerosols: Drop Production from Underwater Bubble Collisions. *Physical Review Letters* **2024**, *133*, 024001.
- (12) Woodcock, A.; Kientzler, C.; Arons, A.; Blanchard, D. Giant condensation nuclei from bursting bubbles. *Nature* **1953**, *172*, 1144–1145.
- (13) Ghabache, E.; Antkowiak, A.; Josserand, C.; Séon, T. On the physics of fizziness: How bubble bursting controls droplets ejection. *Physics of Fluids* **2014**, *26*.
- (14) Joung, Y. S.; Buie, C. R. Aerosol generation by raindrop impact on soil. *Nature Communications* **2015**, *6*, 6083.
- (15) Dubitsky, L.; McRae, O.; Bird, J. C. Enrichment of scavenged particles in jet drops determined by bubble size and particle position. *Physical Review Letters* **2023**, *130*, 054001.
- (16) Yang, Z.; Ji, B.; Ault, J. T.; Feng, J. Enhanced singular jet formation in oil-coated bubble bursting. *Nature Physics* **2023**, *19*, 884–890.
- (17) Zhang, B.; Sanjay, V.; Shi, S.; Zhao, Y.; Lv, C.; Feng, X.-Q.; Lohse, D. Impact forces of water drops falling on superhydrophobic surfaces. *Physical Review Letters* **2022**, *129*, 104501.
- (18) Michon, G.-J.; Josserand, C.; Séon, T. Jet dynamics post drop impact on a deep pool. *Physical Review Fluids* **2017**, *2*, 023601.

- (19) Staffell, I.; Scamman, D.; Abad, A. V.; Balcombe, P.; Dodds, P. E.; Ekins, P.; Shah, N.; Ward, K. R. The role of hydrogen and fuel cells in the global energy system. *Energy & Environmental Science* **2019**, *12*, 463–491.
- (20) Angulo, A.; van der Linde, P.; Gardeniers, H.; Modestino, M.; Rivas, D. F. Influence of bubbles on the energy conversion efficiency of electrochemical reactors. *Joule* **2020**, *4*, 555–579.
- (21) Hodges, A.; Hoang, A. L.; Tsekouras, G.; Wagner, K.; Lee, C.-Y.; Swiegers, G. F.; Wallace, G. G. A high-performance capillary-fed electrolysis cell promises more cost-competitive renewable hydrogen. *Nature Communications* **2022**, *13*, 1304.
- (22) Bashkatov, A.; Park, S.; Demirkir, Ç.; Wood, J. A.; Koper, M. T.; Lohse, D.; Krug, D. Performance enhancement of electrocatalytic hydrogen evolution through coalescence-induced bubble dynamics. *Journal of the American Chemical Society* **2024**, *146*, 10177–10186.
- (23) Shih, A. J.; Monteiro, M. C.; Dattila, F.; Pavesi, D.; Philips, M.; da Silva, A. H.; Vos, R. E.; Ojha, K.; Park, S.; van der Heijden, O.; others Water electrolysis. *Nature Reviews Methods Primers* **2022**, *2*, 84.
- (24) Zhao, X.; Ren, H.; Luo, L. Gas bubbles in electrochemical gas evolution reactions. *Langmuir* **2019**, *35*, 5392–5408.
- (25) Raman, A.; Penas, P.; van der Meer, D.; Lohse, D.; Gardeniers, H.; Rivas, D. F. Potential response of single successive constant-current-driven electrolytic hydrogen bubbles spatially separated from the electrode. *Electrochimica Acta* **2022**, *425*, 140691.
- (26) Sepahi, F.; Verzicco, R.; Lohse, D.; Krug, D. Mass transport at gas-evolving electrodes. *Journal of Fluid Mechanics* **2024**, *983*, A19.

- (27) Bashkatov, A.; Hossain, S. S.; Mutschke, G.; Yang, X.; Rox, H.; Weidinger, I. M.; Eckert, K. On the growth regimes of hydrogen bubbles at microelectrodes. *Physical Chemistry Chemical Physics* **2022**, *24*, 26738–26752.
- (28) Haverkort, J. A general mass transfer equation for gas-evolving electrodes. *International Journal of Hydrogen Energy* **2024**, *74*, 283–296.
- (29) Çayan Demirkır; Wood, J. A.; Lohse, D.; Krug, D. Life beyond Fritz: On the detachment of electrolytic bubbles. 2024; <https://arxiv.org/abs/2406.01989>.
- (30) Park, S.; Liu, L.; Demirkır, Ç.; van der Heijden, O.; Lohse, D.; Krug, D.; Koper, M. T. Solutal Marangoni effect determines bubble dynamics during electrocatalytic hydrogen evolution. *Nature Chemistry* **2023**, *15*, 1532–1540.
- (31) Fernandez, D.; Maurer, P.; Martine, M.; Coey, J.; Möbius, M. E. Bubble formation at a gas-evolving microelectrode. *Langmuir* **2014**, *30*, 13065–13074.
- (32) Hossain, S. S.; Bashkatov, A.; Yang, X.; Mutschke, G.; Eckert, K. Force balance of hydrogen bubbles growing and oscillating on a microelectrode. *Physical Review E* **2022**, *106*, 035105.
- (33) Lubetkin, S. The motion of electrolytic gas bubbles near electrodes. *Electrochimica Acta* **2002**, *48*, 357–375.
- (34) Yang, X.; Baczymalski, D.; Cierpka, C.; Mutschke, G.; Eckert, K. Marangoni convection at electrogenerated hydrogen bubbles. *Physical Chemistry Chemical Physics* **2018**, *20*, 11542–11548.
- (35) Massing, J.; Mutschke, G.; Baczymalski, D.; Hossain, S. S.; Yang, X.; Eckert, K.; Cierpka, C. Thermocapillary convection during hydrogen evolution at microelectrodes. *Electrochimica Acta* **2019**, *297*, 929–940.

- (36) Meulenbroek, A.; Vreman, A.; Deen, N. Competing Marangoni effects form a stagnant cap on the interface of a hydrogen bubble attached to a microelectrode. *Electrochimica Acta* **2021**, *385*, 138298.
- (37) Bashkatov, A.; Hossain, S. S.; Yang, X.; Mutschke, G.; Eckert, K. Oscillating hydrogen bubbles at Pt microelectrodes. *Physical Review Letters* **2019**, *123*, 214503.
- (38) Bashkatov, A.; Yang, X.; Mutschke, G.; Fritzsche, B.; Hossain, S. S.; Eckert, K. Dynamics of single hydrogen bubbles at Pt microelectrodes in microgravity. *Physical Chemistry Chemical Physics* **2021**, *23*, 11818–11830.
- (39) Babich, A.; Bashkatov, A.; Yang, X.; Mutschke, G.; Eckert, K. In-situ measurements of temperature field and Marangoni convection at hydrogen bubbles using schlieren and PTV techniques. *International Journal of Heat and Mass Transfer* **2023**, *215*, 124466.
- (40) Lohse, D.; Zhang, X. Physicochemical hydrodynamics of droplets out of equilibrium. *Nature Reviews Physics* **2020**, *2*, 426–443.
- (41) Young, N.; Goldstein, J. S.; Block, M. The motion of bubbles in a vertical temperature gradient. *Journal of Fluid Mechanics* **1959**, *6*, 350–356.
- (42) Worthington, A. M. XXVIII. On the forms assumed by drops of liquids falling vertically on a horizontal plate. *Proceedings of the Royal Society of London* **1877**, *25*, 261–272.
- (43) Eggers, J.; Sprittles, J. E.; Snoeijer, J. H. Coalescence Dynamics. *Annual Review of Fluid Mechanics* **2024**, *57*.
- (44) Taylor, G. I. The dynamics of thin sheets of fluid. III. Disintegration of fluid sheets. *Proceedings of the Royal Society of London. Series A. Mathematical and Physical Sciences* **1959**, *253*, 313–321.
- (45) Culick, F. E. Comments on a ruptured soap film. *Journal of Applied Physics* **1960**, *31*, 1128–1129.

- (46) Munro, J. P.; Anthony, C. R.; Basaran, O. A.; Lister, J. R. Thin-sheet flow between coalescing bubbles. *Journal of Fluid Mechanics* **2015**, *773*, R3.
- (47) Deike, L.; Ghabache, E.; Liger-Belair, G.; Das, A. K.; Zaleski, S.; Popinet, S.; Séon, T. Dynamics of jets produced by bursting bubbles. *Physical Review Fluids* **2018**, *3*, 013603.
- (48) Gordillo, J.; Rodríguez-Rodríguez, J. Capillary waves control the ejection of bubble bursting jets. *Journal of Fluid Mechanics* **2019**, *867*, 556–571.
- (49) Duchemin, L.; Popinet, S.; Josserand, C.; Zaleski, S. Jet formation in bubbles bursting at a free surface. *Physics of Fluids* **2002**, *14*, 3000–3008.
- (50) Walls, P. L.; Henaux, L.; Bird, J. C. Jet drops from bursting bubbles: How gravity and viscosity couple to inhibit droplet production. *Physical Review E* **2015**, *92*, 021002.
- (51) Sanjay, V.; Lohse, D.; Jalaal, M. Bursting bubble in a viscoplastic medium. *Journal of Fluid Mechanics* **2021**, *922*, A2.
- (52) Gordillo, J. M.; Blanco-Rodríguez, F. J. Theory of the jets ejected after the inertial collapse of cavities with applications to bubble bursting jets. *Physical Review Fluids* **2023**, *8*, 073606.
- (53) Lee, J. S.; Weon, B. M.; Park, S. J.; Je, J. H.; Fezzaa, K.; Lee, W.-K. Size limits the formation of liquid jets during bubble bursting. *Nature Communications* **2011**, *2*, 367.
- (54) Sanjay, V.; Bashkatov, A.; Demirkır, C.; Krug, D.; Lohse, D. Worthington jet injects droplets during coalescence of asymmetric bubbles. *Preprint arXiv* **2024**,
- (55) Lamb, H. *Hydrodynamics*, sixth ed.; Cambridge University Press, 1975.
- (56) Ma, Z.; Duan, L.; Jiang, J.; Deng, J.; Xu, F.; Jiang, L.; Li, J.; Wang, G.; Huang, X.; Ye, W.; others Characteristics and threats of particulate matter from zinc electrolysis manufacturing facilities. *Journal of Cleaner Production* **2020**, *259*, 120874.

Supporting Information:

Electrolyte spraying within H₂ bubbles during water electrolysis

Aleksandr Bashkatov,^{*,†,‡} Florian Bürkle,[¶] Çayan Demirkır,[‡] Wei Ding,[†] Vatsal Sanjay,[‡] Alexander Babich,[†] Xuegeng Yang,[†] Gerd Mutschke,[†] Jürgen Czarske,[¶] Detlef Lohse,^{‡,§} Dominik Krug,[‡] Lars Büttner,[¶] and Kerstin Eckert^{*,†,||}

[†]*Institute of Fluid Dynamics, Helmholtz-Zentrum Dresden-Rossendorf,
Bautzner Landstrasse 400, 01328 Dresden, Germany*

[‡]*Physics of Fluids Group, Max Planck Center for Complex Fluid Dynamics,
MESA+ Institute and J. M. Burgers Centre for Fluid Dynamics, University of Twente,
P.O. Box 217, 7500AE Enschede, Netherlands*

[¶]*Laboratory for Measurement and Sensor System Techniques,
Faculty of Electrical and Computer Engineering, Technische Universität Dresden,
Helmholtzstr. 18, 01069 Dresden, Germany*

[§]*Max Planck Institute for Dynamics and Self-Organization,
Am Fassberg 17, 37077 Göttingen, Germany*

^{||}*Institute of Process Engineering and Environmental Technology,
Technische Universität Dresden, 01062 Dresden, Germany*

E-mail: a.bashkatov@hzdr.de; k.eckert@hzdr.de

1 Bubble dynamics in microgravity environment

Figure 1 demonstrates the evolution of H_2 bubble during water electrolysis at -4 V (vs Pt wire) in 0.5 mol/L H_2SO_4 in a micro- g environment, i.e. at greatly eliminated buoyancy, achieved during the parabolic flights (see Bashkatov et al.¹). The electric current in sub-figure (a) reflects the dynamics of the bubble from its nucleation ($t = -14.71$ s) and until detachment ($t = 2.94$ s). The shadowgraphs in sub-figure (b) depict the bubble position at the time instants marked by red circles in sub-figure (a).

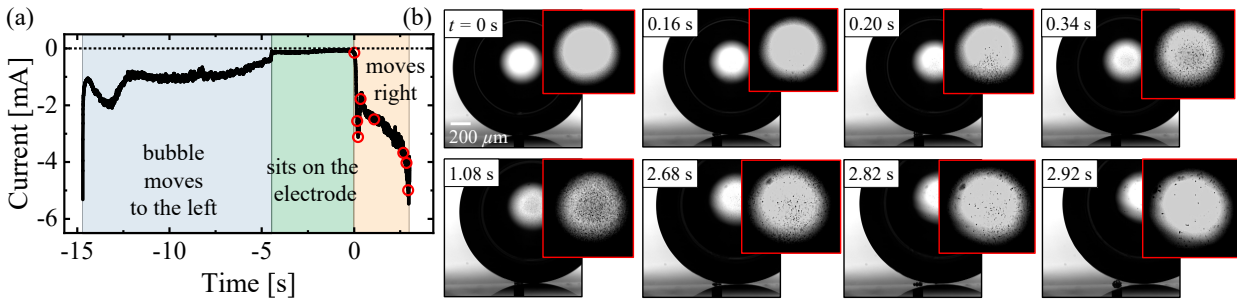


Figure 1: The dynamics of H_2 bubble in micro- g achieved during parabolic flights: (a) electric current over the entire evolution cycle; (b) shadowgraphs of the bubble moving laterally at the instants of time marked by the red circles in (a). The insets zoom into the central part of the bubble.

Here, due to a residual gravitation acceleration and its sign variation, the bubble evolution is characterized by the lateral motion shortly after its nucleation. During the first part of the evolution, it moves to the left (marked by grey shading in Fig. 1a) relative to the electrode center. Later on, it rolls over the electrode moving to the right while continuing to grow via coalescence with the carpet of microbubbles and diffusion. As the bubble rolls over the electrode it blocks most of its active area, minimizing the electric current (marked by green shading in Fig. 1a), hence electrochemical reaction and hydrogen production. The first snapshot ($t = 0$) marks the time instant shortly before the bubble releases the electrode. The insets zoom into the central transparent part of the bubble. From the second snapshot onward, the bubble releases the electrode, drastically increasing the electric current and allowing the formation of a carpet of microbubbles. The mother bubble continuously

coalesces with newly nucleated bubbles (carpet) in the radial direction on a time scale of $\mathcal{O}(\mu\text{s})$. The successive images reveal the internal flow of the microdroplets, emerging from the bottom, presumably at the coalescence spot, and flowing to the top, shortly after coalescence events begin. These droplets can be already seen in the second snapshot ($t = 0.16$ s). Since the bubble is displaced from the electrode center, the coalescence occurring in the radial direction results in the asymmetrical flow. Upon bubble departure, i.e., when no coalescence occurs, the already injected droplets exhibit minimal movement, drifting slowly due to residual velocity. For more details, we refer the readers to the main manuscript.

2 Analytical aberration correction

Aberrations (optical distortions) caused by light refraction at the curved gas-liquid interface of the bubble lead to a significant systematic measurement deviation.²⁻⁴ As the bubbles are of sub-millimeter size, the correction using an optical element is challenging. However, for object-space telecentric lenses, like the microscope objective used for the measurements here, the aberrations can be corrected analytically, which has already been done for the flows inside the droplets.⁵⁻⁷ In the present study, the entrance pupil of the system is at infinity resulting in chief rays parallel to the optical axis in the object space. When back-propagating the rays through the optical system, the intersection of the back-propagated ray and the light sheet (positioned in the middle of the bubble), can be calculated with and without the bubble in the system.

Figure 2 documents a schematic of the chief rays passing through the bubble surface. The solid lines mark the real path of the light scattered at the injected electrolyte droplets, whereas the dashed lines indicate the path recorded by the camera. Fig. 2b demonstrates a single ray passing through the bubble-electrolyte interface with the relevant geometry used in further calculations of the corrected position for each detected droplet. Since the bubble is assumed to be axisymmetric, the position of the droplet is defined by the radial distance

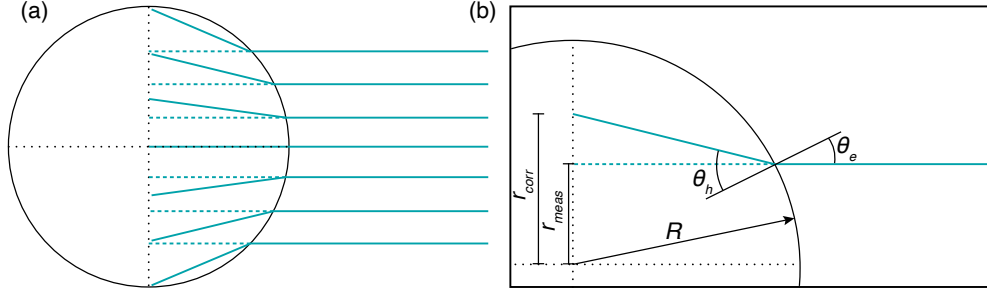


Figure 2: (a) Scheme of the chief rays in an object-space telecentric setup. The microscope objective is on the right side. The solid lines (cyan color) mark the real path of the light, whereas the dashed lines indicate the position in the image plane recorded by the camera. (b) A close view of a single ray passing through the bubble-electrolyte interface with the relevant geometry used in the calculations of the corrected position.

from the bubble center in the plane of the laser sheet. The measured and real (corrected) positions of the injected droplet are therefore defined as r_{meas} and r_{corr} . The corrected position for each of the detected droplets can be calculated as $r_{corr} = r_{meas} + \Delta r$ using

$$\Delta r = \tan \left[\sin^{-1} \left[n \cdot \sin \left[\tan^{-1} \left(\frac{r_{meas}}{\sqrt{R^2 - r_{meas}^2}} \right) \right] \right] - \tan^{-1} \left(\frac{r_{meas}}{\sqrt{R^2 - r_{meas}^2}} \right) \right] \cdot \sqrt{R^2 - r_{meas}^2}, \quad (1)$$

where n is the refractive index of the electrolyte and R is the radius of the bubble.

Figure 3 represents the effect of the correction with (a) showing a raw snapshot of a H_2 bubble and the electrolyte droplets inside; and (b) showing the same snapshot after performing the correction. In the raw image, the droplets are concentrated in the central part of the bubble away from the interface. This is due to the curvature of the bubble, which distorts the path of the rays. This is especially visible at the bottom of the bubble. The light scattered by the microbubble carpet (see manuscript) reaches the camera sensor both directly through the electrolyte and through the bubble. The light traveling through the bubble seems to come from a position closer to the center. When the correction is applied, the light traveling through the bubble seems to come from the bubble surface, which implies

that the analytical model is correct (Fig. 3b). Note that the model assumes a spherical shape

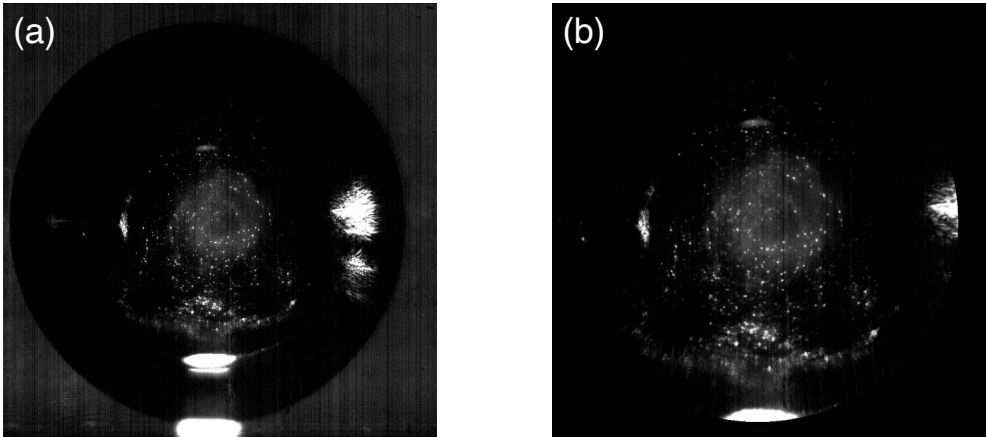


Figure 3: (a) Original snapshot recorded by the camera. (b) Image representing the corrected position of the droplets. The pixels beyond the bubble interface are set to zero (black) in (b).

of the droplet as an approximation. Deviations from the spherical shape of the refracting surface caused e.g. by capillary waves or during detachment can potentially be corrected by approaches using adaptive optics.²⁻⁴

3 Bubble-carpet coalescence prior departure

Figure 4a documents the H_2 bubble shortly before its departure in 0.1 mol/L H_2SO_4 at -2.8 V (vs RHE). The bubble sits above the electrode surface at the carpet of microbubbles having thickness δ and continuously coalesces with it. Figure 4(b-e) zooms in on the central segment of the bubble marked by red rectangular in (a). The image recording was performed at 600 kHz and 720 kHz in (b-d) and (e), respectively.

The high-speed recording demonstrates that some of the droplets are injected at velocities three orders of magnitude larger than a majority of the droplets, especially during the bubble growth phase, reaching up to 15.8 m/s. These events are rather rare and can be observed more frequently shortly before and at the bubble departure, i.e. when the thickness of the carpet is maximum, about $\delta = 16 \mu\text{m}$ and above. The larger δ will also result in droplets of

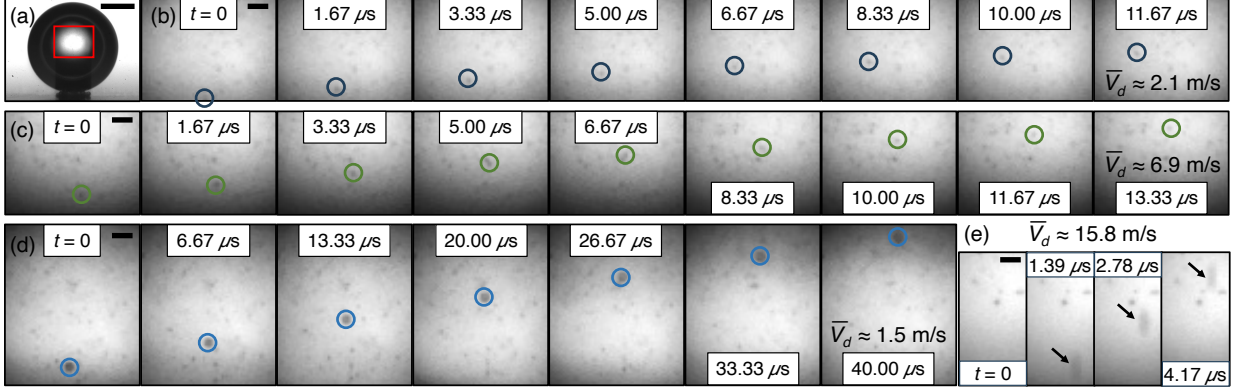


Figure 4: (a) H_2 bubble growing at the electrode at -2.8 V (vs RHE). (b-e) zoom-in on the central segment of the bubble shown by red rectangular in (a), demonstrating the motion of the injected electrolyte droplets with the velocity \bar{V}_d . The image recording was performed at 600 kHz and 720 kHz in (b-d) and (e), respectively. The scale bar is $100 \mu\text{m}$ in (a) and $10 \mu\text{m}$ in (b-e).

bigger size.

4 Stokes's drag: droplet velocity over time upon injection

The model experiment (see Fig. 4 in the main text) demonstrated that the coalescence of two unequal-sized bubbles is followed by an upward liquid jet, known as the Worthington jet, propagating inside of the merging H_2 bubbles. The jet will eventually break into droplet(s) due to the Rayleigh–Plateau instability moving with the velocities of m/s order of magnitude.

In the Stokes regime ($Re < 1$), the injected droplet would experience drag (frictional) force and decelerate quickly due to viscous drag within the surrounding H_2 gas. For reference, the Reynolds number given as $Re = (\rho_{\text{H}_2} \cdot V_d \cdot 2R_d) / \mu_{\text{H}_2}$ equals to 0.5 with the radius of the droplet $R_d = 5 \mu\text{m}$ and velocity of the droplet $V_d = 5$ m/s. ρ_{H_2} and μ_{H_2} are the density and dynamic viscosity of the hydrogen. We apply Newton's second law to the drag force,

$$m_d \cdot \frac{dV_d}{dt} = F_{drag} = -6 \cdot \pi \cdot \mu_{\text{H}_2} \cdot R_d \cdot V_d, \quad (2)$$

where m_d is the mass of the droplet. By integrating Eq. 2, the velocity of the droplet over time reads

$$V_d(t) = V_0 \cdot \exp(-t/\tau_d), \quad (3)$$

where $\tau_d = \frac{m_d}{6\pi\mu_{H2}R_d}$ and V_0 is an initial droplet velocity at the separation from the jet. Typically, $\tau_d \approx 25 \mu s$ ($R_d = 1 \mu m$) and $\tau_d \approx 650 \mu s$ ($R_d = 5 \mu m$), so drag quickly brings the flying drop to a stand-still.

Figure 5 demonstrates (a) the velocity $V_d(t)$ and (b) the traveled distance $S_d(t) = \int_0^t V_d(t') dt'$ of the injected droplet over time at three various sizes of $R_d = 1 \mu m$, $R_d = 3 \mu m$, and $R_d = 5 \mu m$, plotted in black, red, and blue colors, respectively and with the initial velocities of $V_0 = 0.5 \text{ m/s}$ and $V_0 = 5 \text{ m/s}$ at $t_0 = 0$, plotted as solid and dotted lines, respectively. $S_d(t)$ is calculated by integrating the $V_d(t)$ in subfigure (a). Both plots are on a semi-logarithmic scale.

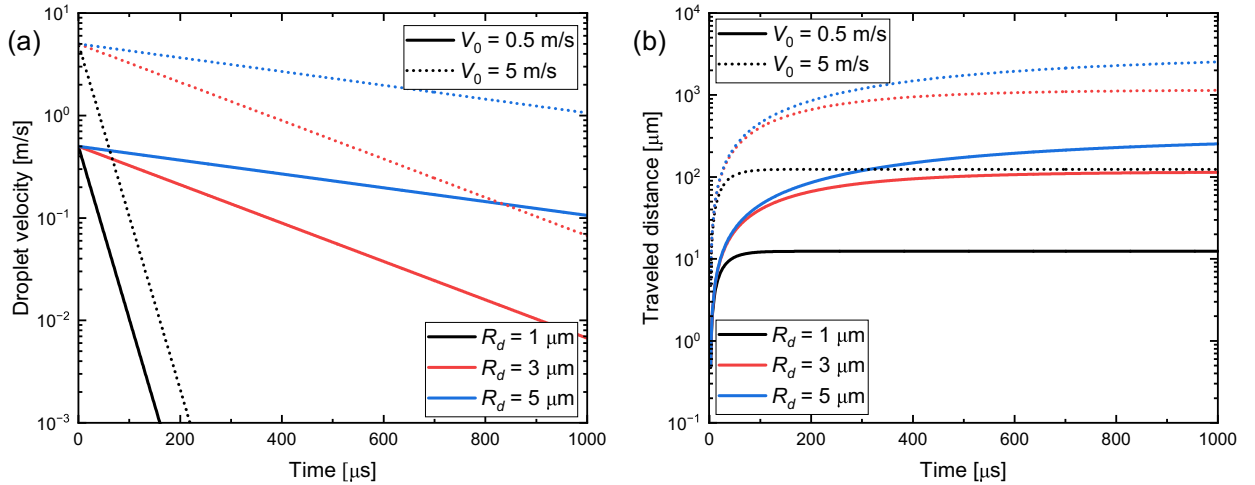


Figure 5: (a) Velocity (V_d) and (b) traveled distance (S_d) of the injected droplet over time.

Upon the injection, the droplet velocity thus decays exponentially with time. The droplet with $R_d = 1 \mu m$ (implies $\tau_d \approx 25 \mu s$) and with $V_0 = 5 \text{ m/s}$ slows down to the velocity of 10^{-2} m/s at $t = 160 \mu s$ by travelling $S_d = 124 \mu m$. In comparison, by reducing the initial

injection velocity (V_0), the droplet will reach the same order of magnitude (10^{-2} m/s) at $t = 100 \mu\text{s}$ by traveling only $S_d = 12 \mu\text{m}$. By increasing the droplet size from $R_d = 1 \mu\text{m}$ to $R_d = 3 \mu\text{m}$ and $R_d = 5 \mu\text{m}$, the effect of viscous drag progressively reduces, so that the droplet at $V_0 = 5$ m/s can cover distances larger than 1 mm before the final position is reached (see subfigure b).

The droplet velocity V_d of 10^{-2} mm/s order of magnitude approximately resembles the one found in Fig. 2 (main text) at the bubble bottom in the bubble-carpet system.

While it is a non-trivial to identify the injection time due to continuous bubble-carpet coalescence events start shortly upon bubble nucleation, i.e. after the formation of a single bubble at the electrode surface, we hypothesize that the velocity is resolved away from the injection area at the distance somewhat in between the above-mentioned cases $S_d = 12 \mu\text{m}$ and $S_d = 100 \mu\text{m}$. Rather, it is closer to the $S_d = 12 \mu\text{m}$ and therefore we tend to assume the initial velocity is close to $V_0 = 0.5$ m/s.

This approximately resembles the velocity of the droplets ($R_d = 1 \mu\text{m}$) in Fig. 2 (main text) resolved at approx. the same distance away from the injection cross-section at the bubble bottom in the bubble-carpet system.

Besides the initial conditions such as the size ratio of two coalescing bubbles and broken symmetry of the coalescence as in the case of the bubble-carpet system (Figs. 1 and 2 in the main text), the initial velocity of the droplet will depend on at which moment the droplet separates from the jet, i.e. whether it is the first or second droplet as in case of Fig. 4 (see main text). The last separation happened at the retraction of the jet, and therefore with a much smaller velocity, at 1.1 m/s and $R_d = 11 \mu\text{m}$ for the second droplet vs 7.4 m/s and $R_d = 7 \mu\text{m}$ for the first droplet. The solution is not trivial, since the first droplets are of smaller size than the last ones, and therefore slows down much faster, however, separating at a much faster initial velocity V_0 .

In the case of the surface-attached bubble (Fig. 3, main text), the injected droplet slows down upon the injection due to the Stokes's drag and then falls at the bubble-electrode

contact area due to gravitational forces, presumably with the terminal velocity. In the Stokes regime ($Re < 1$), the terminal velocity of the droplet can be written

$$V_t = \frac{2}{9} \frac{R_d^2 \Delta \rho g}{\mu_{H_2}}, \quad (4)$$

where $\Delta \rho = \rho_{el} - \rho_{H_2}$ is the electrolyte-gas density difference and μ_{H_2} the dynamic viscosity of the hydrogen. Given that the second observed droplet has a radius of about $r = 4 \mu\text{m}$, the terminal velocity $V_t = 4.1 \text{ mm/s}$. This value closely correlates with the experimentally estimated velocity of $\bar{V}_d = 6 \text{ mm/s}$ during the period from $t = 1.33 \text{ ms}$ after injection until the droplet reaches the bubble-electrode contact area at $t = 86.67 \text{ ms}$.

5 Mechanism of injection: experiment vs simulation

The direct numerical simulation accurately reproduces the key features and timescales of phenomena such as neck formation, capillary wave propagation, jet formation, and droplet breakup. We then proceed to compare the details of drop ejection between the experiments and simulations presented in the manuscript body in Fig. 4. In the experiments, the first droplet with a radius of $R_d = 13 \mu\text{m}$ is observed at $t = 250.0 \mu\text{s}$ and ejects with a velocity of approximately 7.2 m/s . The second droplet, with a radius of $R_d = 24 \mu\text{m}$, appears at $t = 341.7 \mu\text{s}$ and separates just before the jet starts to retract between $t = 333.3 \mu\text{s}$ and $t = 341.7 \mu\text{s}$, resulting in a much smaller velocity of about 1.1 m/s . In contrast, in the simulations, the first droplet (radius $R_d = 15 \mu\text{m}$) pinches off at $t = 260 \mu\text{s}$ with a velocity of $\bar{V}_d = 4.3 \text{ m/s}$. The second droplet (radius $R_d = 18 \mu\text{m}$) pinches off at $t = 285 \mu\text{s}$ with a velocity of $\bar{V}_d = 3.4 \text{ m/s}$. Additionally, another droplet (radius $R_d = 3 \mu\text{m}$) was detected at an earlier phase ($t = 208 \mu\text{s}$) with a much faster velocity of $\bar{V}_d = 43 \text{ m/s}$, likely due to numerical artifacts caused by finite mesh resolution. This droplet can be barely seen in Fig. 4 (main manuscript) at $t = 208 \mu\text{s}$. The characteristics of the injected droplets are summarised

in Table 1.

Table 1: Comparison of the droplet injection characteristics between experiment and simulations. t represents the time from the onset of coalescence, R_d and \bar{V}_d the radius and the velocity of the injected droplet, respectively. In the experiment, only two droplets (#1 and #2) are observed, whereas the simulation shows three droplets (#0, #1, and #2). Droplet #0 is likely resolved due to numerical artifacts caused by finite mesh resolution.

Droplet [#]	t [μs]		R_d [μm]		\bar{V}_d [m/s]	
	experiment	simulation	experiment	simulation	experiment	simulation
0	-	208	-	3	-	43
1	250	260	13	15	7.2	4.3
2	341.7	285	24	18	1.1	3.4

The comparison shows qualitative agreement between experiments and simulations, though quantitative discrepancies remain. Experimental estimates of droplet size and velocity may be slightly inaccurate due to the bubble curvature, which could be analytically corrected for a spherical shape. However, the merged bubble deforms significantly upon droplet injection which complicates precise measurements. We stress that the breakup process is a finite-time singularity,⁸ naturally leading to a qualitative agreement between experiments and simulations. However, the time to break up and the velocity of the ejected drop are sensitive to the discrete nature of simulation equations and experimental noise or measurement technique.⁹ Additionally, the jet’s velocity, which determines the droplet’s post-ejection velocity, varies over time;^{10,11} small variations in sampling time can thus explain discrepancies. Factors such as an inaccurate gas-liquid viscosity ratio and the sensitivity of velocity to the Ohnesorge number and size ratio also contribute to the differences between experimental and simulation results.¹² Given these error sources, the observed discrepancies are reasonable.

References

- (1) Bashkatov, A.; Yang, X.; Mutschke, G.; Fritzsche, B.; Hossain, S. S.; Eckert, K. Dynamics of single hydrogen bubbles at Pt microelectrodes in microgravity. *Physical Chemistry*

Chemical Physics **2021**, *23*, 11818–11830.

- (2) Bilsing, C.; Nützenadel, E.; Burgmann, S.; Czarske, J.; Büttner, L. Adaptive-optical 3D microscopy for microfluidic multiphase flows. *Light: Advanced Manufacturing* accepted article preview 11 July, 2024.
- (3) Gao, Z.; Radner, H.; Büttner, L.; Ye, H.; Li, X.; Czarske, J. Distortion correction for particle image velocimetry using multiple-input deep convolutional neural network and Hartmann-Shack sensing. *Optics Express* **2021**, *29*, 18669–18687.
- (4) Radner, H.; Stange, J.; Büttner, L.; Czarske, J. Field-programmable system-on-chip-based control system for real-time distortion correction in optical imaging. *IEEE Transactions on Industrial Electronics* **2020**, *68*, 3370–3379.
- (5) Kang, K. H.; Lee, S. J.; Lee, C. M.; Kang, I. S. Quantitative visualization of flow inside an evaporating droplet using the ray tracing method. *Measurement Science and Technology* **2004**, *15*, 1104.
- (6) Minor, G.; Oshkai, P.; Djilali, N. Optical distortion correction for liquid droplet visualization using the ray tracing method: further considerations. *Measurement Science and Technology* **2007**, *18*, L23.
- (7) Minor, G.; Djilali, N.; Sinton, D.; Oshkai, P. Flow within a water droplet subjected to an air stream in a hydrophobic microchannel. *Fluid Dynamics Research* **2009**, *41*, 045506.
- (8) Zeff, B. W.; Kleber, B.; Fineberg, J.; Lathrop, D. P. Singularity dynamics in curvature collapse and jet eruption on a fluid surface. *Nature* **2000**, *403*, 401–404.
- (9) Eggers, J.; Sprittles, J. E.; Snoeijer, J. H. Coalescence Dynamics. *Annual Review of Fluid Mechanics* **2024**, *57*.

- (10) Deike, L.; Ghabache, E.; Liger-Belair, G.; Das, A. K.; Zaleski, S.; Popinet, S.; Séon, T. Dynamics of jets produced by bursting bubbles. *Physical Review Fluids* **2018**, *3*, 013603.

- (11) Sanjay, V.; Lohse, D.; Jalaal, M. Bursting bubble in a viscoplastic medium. *Journal of Fluid Mechanics* **2021**, *922*, A2.

- (12) Walls, P. L.; Henaux, L.; Bird, J. C. Jet drops from bursting bubbles: How gravity and viscosity couple to inhibit droplet production. *Physical Review E* **2015**, *92*, 021002.